To be submitted to J. Mech. Phys. Solids (January, 2000)

New differential effective medium theory for the linear elastic moduli of a material containing composite inclusions

E.J. Garboczi
National Institute of Standards and Technology
Building Materials Division
100 Bureau Drive, Stop 8621
Gaithersburg, Maryland 20899-8621 USA

J.G. Berryman
Lawrence Livermore National Laboratory
P. O. Box 808 L-200
Livermore, CA 94551-9900

Abstract

Concrete is a good example of a composite material in which the inclusions (rocks and sand) are surrounded by a thin shell of altered matrix material and embedded in a normal matrix. Concrete therefore may be viewed as consisting of a matrix material containing composite inclusions. Assigning each of these phases different linear elastic moduli results in a complicated effective elastic moduli problem.

A new kind of differential effective medium theory (D-EMT) is presented in this paper that is intended to address this problem. The key new idea is that each inclusion particle, surrounded by a shell of another phase, is mapped onto an effective particle of uniform elastic moduli. The resulting simpler composite, with a normal matrix, is then treated in usual D-EMT. Before use, however, the accuracy of this method must be determined, as effective medium theory of any kind is an uncertain approximation. One good way to assess the accuracy of effective medium theory is to compare to exact results for known microstructures and phase moduli. Exact results, however, only exist for certain microstructures (e.g., dilute limit of inclusions) or special choices of the moduli (e.g., equal shear moduli). Recently, a special finite element method has been described that can compute the linear elastic moduli of an arbitrary digital image in 2-D or 3-D. If a random microstructure can be represented with enough resolution by a digital image, then the elastic moduli of the random microstructure can be readily computed. This method is used, after proper error analysis, to provide stringent tests of the new D-EMT equations, which are found to compare favorably to numerically exact finite element simulations, in both 2-D and 3-D, with varying composite inclusion particle size distributions.

1 Introduction

Concrete is a composite material. A typical recipe contains a cement paste matrix and inclusion particles of various sizes, ranging from the smallest sand grains of diameter 100μm, to the largest rocks of diameter 10 mm to 20 mm. However, upon closer examination, one finds that the presence of the grains in the paste changes a thin layer of matrix material surrounding each inclusion. The cement paste matrix in this shell is different, usually more porous, than the bulk of the surrounding cement paste matrix. Typical widths of this layer are in the range 10 μm to 30 μm [1–3].

Concrete therefore consists of at least three distinct types of constituents. If the altered shell of matrix material is associated with the grains, then the point of view may be taken (and this will become our point of view) that concrete consistes of a matrix material containing *composite* inclusions. Assigning each of these phases different linear elastic moduli results in a complicated effective elastic moduli problem.

In fact, the problem is still more complicated. The "shell" around each inclusion has a gradient of properties, since the cement paste matrix is least dense at the particle surface and increases outwards to the full matrix density [2, 4, 5]. The dilute limit, with a single spherical inclusion surrounded by a spherically symmetric gradient of elastic properties, can be handled exactly [6–9]. But the real microstructure of concrete, with a wide particle size distribution of inclusions, each surrounded by overlapping gradients of properties, is too difficult to treat analytically, by numerical methods, or by effective medium theory (EMT). However, it has been shown that a multi-scale model can be used in order to map this very complicated microstructure into a simpler, but still complicated, microstructure, where the shell layers can be treated theoretically as having uniform properties [6, 10, 11]. The three phase composite described above then becomes appropriate for the concrete elastic moduli problem.

Differential effective medium theory (D-EMT) for this microstructure has been developed previously in several ways [12–17]. Predictions for the electrical properties of this microstructure have recently been checked against random walk simulations [18,19]. These simulations are accurate and simple, but time-consuming, hence the need for effective medium theory. The most accurate D-EMT for this application was developed using a new idea in differential effective medium theory (D-EMT) [19]. The key idea was that a spherical inclusion, along with its surrounding thin shell of altered matrix material, was exactly mapped into a new, slightly larger homogenized inclusion, which included the hard but poorly conducting particle and the softer but better conducting shell, and which had a uniform conductivity. The new system of effective particles embedded in the matrix could then be treated easily using a differential effective medium theory (D-EMT).

A rather different approach to three-phase effective medium theory could be based on the self-consistent formulas of Christensen and Lo [20, 21], but as we shall show the method presented here has considerably more flexibility in the range of complex microstructures that can be incorporated into the model.

This new kind of D-EMT is extended to linear elastic properties in this paper. Similar to the idea used for conductivity, a spherical inclusion, with a surrounding shell layer, is mapped onto an effective particle of uniform elastic moduli. The problem then becomes a simple composite composed of spherical particles, of varying sizes and elastic moduli, embedded in a uniform matrix. This composite can then be treated in the usual D-EMT.

Except for some special models [22], the accuracy of most EMTs is often in doubt. From the point of view of tailoring the approximation to the specific material microstrcture that we want to model, EMTs of any kind tend to be uncontrolled approximations. Checking the accuracy of an EMT by comparing its predictions to experimental results is inadequate from the theoretical point of view because the microstructure and phase elastic moduli are usually only approximately known. Observed discrepancies could be from the EMT, or equally well could arise from the approximate knowledge of the experimental material. A more satisfactory way of assessing the accuracy of EMT is to compare to essentially exact (computational) results, where microstructure and phase moduli are controlled by the user.

But exact elastic results for non-trivial microstructures are rather rare, and only exist for certain microstructures (e.g., dilute limit of inclusions) or special choices of the moduli (e.g., equal shear moduli) [23, 24]. In the case of conductivity, the D-EMT results could be checked on model concrete microstructures using accurate random walk simulations [19]. Recently, a special finite element method has been described that can compute the linear elastic moduli of an arbitrary digital image in 2-D or 3-D [25]. This method is used, after proper error analysis, to provide stringent tests of the new D-EMT equations. The results are found to compare favorably with the essentially exact finite element calculations, in both 2-D and 3-D, with a variety of simple inclusion size distributions.

2 Differential effective medium theory and effective particle mapping

D-EMT [26, 27] was chosen as the best candidate for the composite inclusion problem for the following reason. The accuracy of an EMT is often linked to how well its percolation properties match those of the experimental system being considered [18, 28, 29]. In D-EMT, the inclusions are always discontinuous, and the matrix is always continuous. Concrete has the same properties since the granular aggregate is fully surrounded by the cementing matrix material. Thus, the microstructures of the theory and the problem of interest are well matched. Furthermore, we want to be able to incorporate a range of sizes of particles into the theory in a controlled way. It is not clear how to do this in a self-consistent three-component model [20], but we will show that this is not difficult to achieve with the present approach.

The standard D-EMT is a two-phase theory, or rather two topological phases, since each inclusion can be a different phase by having different elastic properties. In the present case, the thin shell of disturbed material around each granular inclusion causes conceptual problems for D-EMT, since it introduces at least one more topological phase. To make use of D-EMT in this setting, the question arises whether this shell should be treated as part of the inclusion, or as part of the matrix?

One answer to this conceptual dilemma is to construct versions of D-EMT in which the shell regions are either unambiguously inclusion or matrix. Since the shell regions, disregarding overlaps between shells, will necessarily assume the same shape as the spherical inclusion particles, the option of making the shell regions part of the inclusions seems a most appropriate one. This is accomplished by mapping each inclusion particle together with its accompanying shell into a single effective particle, with size sufficient to incorporate both and with uniform elastic properties. This idea is illustrated in Fig. 1, and will be developed more fully below. Thus, the effective medium theory that we develop will be for a material having a matrix that contains composite inclusions.

2.1 Standard D-EMT

In the usual D-EMT [27], when a particle with elastic moduli K_p and G_p is embedded in a matrix with elastic moduli K_m and G_m, the dilute limit is used to generate an approximate equation that can be solved for the effective elastic moduli [27]. In the dilute limit, the value of c, the volume fraction of particles, is small enough so that the particles do not influence each other. The effective elastic moduli, K and G, are then given by [30]:

$$K = K_m + K_m k c + O(c^2), \tag{1}$$

$$G = G_m + G_m g c + O(c^2), \tag{2}$$

where k and g are dimensionless coefficients. These coefficients are often called the dilute limit slopes or the intrinsic moduli [31], and are functions of both the shape of the particle, and the ratios $\frac{K_p}{K_m}$ and $\frac{G_p}{G_m}$. The higher order terms in the c expansion come from interactions between particles, and so are negligible in the dilute limit.

For circular particles in a 2-D matrix and spherical particles in a 3-D matrix, these dilute limits are known. For circular particles in 2-D, the values of k and g are:

$$k = \frac{(K_m + G_m)(K_p - K_m)}{K_m(K_p + G_m)}, \tag{3}$$

$$g = \frac{2(K_m + G_m)(G_p - G_m)}{G_m(K_m + G_p) + G_p(K_m + G_m)}. \tag{4}$$

For spherical particles in 3-D, the values of k and g are:

$$k = \frac{(K_m + \frac{4}{3}G_m)(K_p - K_m)}{K_m(K_p + \frac{4}{3}G_m)}, \tag{5}$$

$$g = \frac{5(K_m + \frac{4}{3}G_m)(G_p - G_m)}{3G_m(K_m + \frac{8}{9}G_m) + 2G_p(K_m + 2G_m)}. \tag{6}$$

The dilute limits are now used to generate approximate differential equations suitable to estimate the elastic moduli when arbitrary amounts of the included phase are introduced into the matrix. Suppose that a non-dilute volume fraction c of particles have been placed in the matrix. The effective elastic moduli of the entire composite system are now $K(\phi)$ and $G(\phi)$, where $\phi = 1 - c$ is the matrix volume fraction. The resulting system of matrix plus particles is treated as a homogeneous material. Suppose then that additional particles are added by removing a differential volume element, dV, from the homogeneous material, and replacing it by an equivalent volume of the inclusion phase. The new elastic moduli, $K + dK$ and $G + dG$, are given in the dilute limit by

$$K + dK = K + K\,k(K, G)\frac{dV}{V}, \tag{7}$$

$$G + dG = G + G\,g(K, G)\frac{dV}{V}, \tag{8}$$

where V is the total volume and $k(K, G)$ and $g(K, G)$ are the same quantities as those in eqs. (1) and (2), but with the replacement $K_m \to K$ and $G_m \to G$. This is the key approximation that is made in order to generate the standard two-component D-EMT. When the volume element dV was removed, only a fraction ϕ was actually matrix material, so that the actual change in the matrix volume fraction, $d\phi$, is given by

$$d\phi = -\phi \frac{dV}{V}. \tag{9}$$

Making this substitution, eq. (8) then reduces to the coupled set of equations

$$\begin{aligned} \frac{dK}{d\phi} &= -kK/\phi, \\ \frac{dG}{d\phi} &= -gG/\phi. \end{aligned} \tag{10}$$

These equations are coupled via the k and g terms, which depend on the values of K and G for the matrix at the given value of ϕ.

The above has been written for a single size inclusion. For a size distribution of inclusion particle diameters $\{b_j\}$, the theory is only slightly more complicated. Some composites might also have different elastic moduli for different sizes of particles. A general way of characterizing the inclusion size distribution is by specifying the diameter of each type, d_j, $j = 1, M$, where M is the number of different kinds of particles, and f_j is the fraction of the total inclusion volume that is taken up by the j-th kind of particle, with $\sum_j f_j = 1$. The elastic moduli of the j-th kind of particle is given by K_j and G_j.

In fact, it makes some difference to the final results just how (*i.e.*, in what order) the various inclusion types are mixed into the composite [14]. We have chosen to assume the inclusion distribution is maintained as a fixed quantity throughout the mixing process. The way this affects the D-EMT is seen in the dilute limit, or the values of k and g, which become $\langle k \rangle = \sum_j f_j k_j$ and $\langle g \rangle = \sum_j f_j g_j$. These slopes are first averaged over the inclusion particle size distribution before being used in the formula for the dilute limit. The D-EMT is then built up the same way as for a single kind of particle, but using the average slopes.

2.2 Effective particle mapping

It has been long known that a spherical particle, surrounded by a spherical shell of different elastic moduli, can be exactly mapped into a new, uniform property spherical particle, which is as large as the old particle plus shell combined [21, 32, 33]. This can also be done for a circular particle surrounded by a circular shell.

Let the interior particle be phase 3, with diameter b, and the shell material be phase 2, with outer diameter a. The phase label 1 is reserved for the matrix. Figure 1 shows a schematic of such a mapping. Ref. [33] contains the formulas for such a mapping in 3-D, for both the effective properties K and G, and for G in 2-D. The 2-D mapping for K is also included below. Note that in Ref. [33], in 3-D, label i is the same as 3 here, and label m is the same as 2 here. In 2-D, label f is the same as 3 here, and label m is the same as 2 here. Also, in both 2-D and 3-D, ν_i is the Poisson's ratio for phase i.

The 3-D results are presented first. The effective G is the solution to the following quadratic equation (taking the positive square root),

$$A(G/G_2)^2 + 2B(G/G_2) + C = 0 \tag{11}$$

with the coefficients given by:

$$\begin{aligned} A &= 8z(4-5\nu_2)\eta_1 p^{10/3} - 2[63z\eta_2 + 2\eta_1\eta_3]p^{7/3} + 252z\eta_2 p^{5/3} - \\ &\quad 50z(7-12\nu_2+8\nu_2^2)\eta_2 p + 4(7-10\nu_2)\eta_2\eta_3, \\ B &= -2z(1-5\nu_2)\eta_1 p^{10/3} + 2[63z\eta_2 + 2\eta_1\eta_3]p^{7/3} \\ &\quad -252z\eta_2 p^{5/3} + 75z(3-\nu_2)\eta_2\nu_2 p + \frac{3}{2}(15\nu_2 - 7)\eta_2\eta_3, \\ C &= 4z(5\nu_2 - 7)\eta_1 p^{10/3} - 2[63z\eta_2 + 2\eta_1\eta_3]p^{7/3} \\ &\quad +252z\eta_2 p^{5/3} + 25z(\nu_2^2 - 7)\eta_2 p - (7+5\nu_2)\eta_2\eta_3, \\ \eta_1 &= z(7-10\nu_2)(7+5\nu_3) + 105(\nu_3 - \nu_2), \\ \eta_2 &= z(7+5\nu_3) + 35(1-\nu_3), \end{aligned}$$

$$\eta_3 = z(8 - 10\nu_2) + 15(1 - \nu_2),$$
$$z = G_3/G_2 - 1,$$
$$\text{and} \quad p = (b/a)^3.$$

Note that the subscripts 1, 2, and 3 for the η_i variables should not be confused with the phase labels.

The effective K is given by:

$$K = K_2 + \frac{c(K_3 - K_2)}{1 + (1 - c)\frac{(K_3 - K_2)}{(K_2 + \frac{4}{3}G_2)}} \tag{12}$$

For 2-D, the plane strain shear modulus, μ_{23}, is used from Ref. [33], but with the notation of this paper. The effective G is given by the solution of the following quadratic equation (taking the negative square root),

$$A(G/G_2)^2 + 2B(G/G_2) + C = 0 \tag{13}$$

with the coefficients given by:

$$A = 3p(1-p)^2(r-1)(r+\eta_3) + [r\eta_2 + \eta_2\eta_3 - (r\eta_2 - \eta_3)p^3][p\eta_2(r-1) - (r\eta_2 + 1)],$$
$$B = -3p(1-p)^2(r-1)(r+\eta_3) + \frac{1}{2}[r\eta_2 + (r-1)p + 1][(\eta_2 - 1)(r+\eta_3) - 2(r\eta_2 - \eta_3)p^3]$$
$$+\frac{p}{2}(\eta_2 + 1)(r-1)[r + \eta_3 + (r\eta_2 - \eta_3)p^3],$$
$$C = 3p(1-p)^2(r-1)(r+\eta_3) + [r\eta_2 + (r-1)p + 1][r + \eta_3 + (r\eta_2 - \eta_3)p^3],$$
$$\eta_i = 3 - 4\nu_i, \quad \text{for} \quad i = 2, 3,$$
$$r = G_3/G_2,$$
$$\text{and} \quad p = (b/a)^2.$$

The effective K is given by:

$$K = \frac{p(K_2 + G_2)K_3 + (1-p)(K_3 + G_2)k_2}{p(K_2 + G_2) + (1-p)(K_3 + G_2)}. \tag{14}$$

2.3 New D-EMT

The resulting effective particle is now be treated as the inclusion phase in usual D-EMT, as described above. When an inclusion particle size distribution is used, the functions $k(K, G)$ and $g(K, G)$ are averages over this size distribution, as was stated above. The differential equations can be easily solved numerically by a 4th order Runge-Kutta method [34, 35].

There are a few differences, however, involving the effective inclusion volume fraction. Each particle is now of diameter $a_j = b_j + h_j$, where h_j is the shell thickness for the j-th kind of inclusion, so that the volume fraction of "effective inclusions" now goes to the renormalized value c', not c. The value of c' must be known in order to know where to terminate integration of the D-EMT differential equations, which start at $c' = 0$.

These differences can be determined simply by considering the number of particles of a certain type. If V_j is the total volume of the j-th kind of particle, and N_j is the total number of this kind of particle, then

$$N_j \frac{\pi}{6}(b_j)^3 = V_j, \tag{15}$$

and, therefore,

$$\frac{N_j}{V}\frac{\pi}{6}(b_j)^3 = \frac{V_j}{V} = f_j\, c, \tag{16}$$

$$n_j \frac{\pi}{6}(b_j)^3 = f_j\, c, \tag{17}$$

where V is the total volume of the system and n_j is the number of particles of type j per unit total material volume.

Now the new values of f_j and c, f_j' and c', are defined by rewriting the previous equation:

$$n_j \frac{\pi}{6} a_j^3 = f_j' \, c'. \tag{18}$$

The values of f_j' and c' can also be defined directly by

$$c' = \sum_{j=1}^{M} n_j \frac{\pi}{6} a_j^3, \tag{19}$$

$$f_j' = \frac{n_j a_j^3}{\sum_{i=1}^{M} n_i a_i^3}. \tag{20}$$

Combining the above equations, we can then derive forms for f_j' and c' that involve only f_j, c, and $\alpha_j = a_j^3/b_j^3$:

$$f_j' = \frac{f_j \alpha_j}{\sum_{i=1}^{M} f_i \alpha_i}, \tag{21}$$

$$c' = c \sum_{j=1}^{M} f_j \alpha_j. \tag{22}$$

It should be noted that while the value of c was for non-overlapping aggregate particles, the value of c' is for the volume occupied by each aggregate particle and its surrounding shell, where the shell layers are assumed to not overlap. In a real concrete, these shells do overlap, which can cause percolation phenomena [36]. This treatment of the shell volume fraction is another approximation of the D-EMT method. In the numerical results described in the next section chosen to check the D-EMT, the shell regions actually do not overlap, and therefore are consistent with the assumptions built into the theory.

In summary, a D-EMT calculation is performed as follows. First all the different kinds of composite inclusions are mapped to effective particles, with new moduli and sizes. Next the inclusion particle size distribution is used to compute c' and f_j'. Then the differential equations in eqs. (5) are solved numerically using a 4th order Runge-Kutta method, where the slopes $\langle k \rangle$ or $\langle g \rangle$ are averaged over the effective particle size distribution f'_j. Note that for spherical particles, the new diameters of the effective particles, a_j, do not come in explicitly into any of the equations for k and g, but only in the definitions of f'_j and c'. For many materials, including concrete, the inclusion particle size distribution is given by a sieve analysis, where partial volume fractions f_j refer to the amount lying inside a certain diameter range. This case can be easily converted to the one considered here, by dividing each range into several points, and dividing up the volume in that range appropriately. The actual FORTRAN software used to calculate the D-EMT results in this paper is available on the Internet [37].

3 Finite Element Computations

A recent finite element method for digital images [25] was used to generate data with which to check the results of the D-EMT. Of course, the most important question is: how accurate are the finite element method results? Since these results are for concentrated, random systems, there are no exact analytical data against which to check the numerical results. Fortunately, by careful consideration of the possible sources of errors, one can establish the accuracy of the numerical data.

These numerical computations are carried out by first generating the random microstructure desired by building a digital image, in 2-D or 3-D. Each pixel is then treated as a bi-linear element (2-D) or tri-linear element (3-D), so that the entire digital lattice is treated as the finite element mesh. The elastic equations are written as a variational principle, which is then minimized over the digital lattice. The effective moduli are usually defined by a stress average, although they could be defined by an energy average [24].

Because of the structure of the algorithm, there are three main sources of error. These include: (1) finite size effect, (2) digital resolution, and (3) statistical variation [38].

The finite size effect comes about because any given digital image, even with periodic boundary conditions, can only represent a small part of a large random solid. Here we are thinking of inclusions embedded in a matrix. There can be errors induced if the sample is not large enough to possess enough inclusions to be statistically representative. This sampling error can be assessed by running several different size samples, and seeing whether the results change between system sizes. In the samples considered, the inclusion size, in terms of pixels, stays the same, so that samples having larger lattices contain more inclusions.

The digital resolution error comes from using square or cubic pixels to represent the inclusions. Even if the inclusions had the same shape as the digital lattice, there would still be a resolution error since one is representing continuum equations with a digital lattice. The size of this error can be checked by holding the number of inclusions constant, and varying the size of the lattice so that there are more or less pixels per unit length.

The statistical variation error source simply comes about because the systems under consideration are random ones. Therefore, for a given concentration of inclusions, there are many ways in which the inclusions might be randomly arranged. Each arrangement will have somewhat different elastic moduli, in general. The size of this source of error can be assessed by computing the elastic moduli of several different realizations of the same system (same size lattice, same number of inclusions).

Figure 2 shows the 2-D 1000^2 systems that were used to check the D-EMT results. There were three sizes of inclusions. On a 1000^2 size digital lattice, these had outer-inner diameters, in pixels, of $121-99$, $91-69$, and $61-39$. The experience of many previous results had shown that having the diameter of the largest inclusion less than one-eighth of the size of the unit cell would make any finite size effects negligible. Holding the number of inclusions fixed, runs were made at sizes of 500^2 and 2000^2, with only $1-2\%$ variation, so that the size used for all the runs was 1000^2. The statistical variation for 1000^2 size systems was very small, and so was neglected.

The inner particle had Young's modulus $E_3 = 5.0$ and Poisson's ratio $\nu_3 = 0.2$, the matrix had $E_1 = 1.0$ and $\nu_1 = 0.3$, while the shell had $\nu_2 = 0.3$ and a Young's modulus that ranged from 0.1 to about 10.0. Two systems were chosen, with matrix area fractions of about 0.3

and 0.5. Exact details of the microstructures considered are displayed in Tables 1 and 3. These details are given for future reference, as the results are almost unique in being highly accurate results for random, non-dilute systems.

In 3-D, there were two systems considered. The first used only one size of composite sphere, with a ratio of outer to inner diameters of 1.75. The ratio of the unit cell size compared to the particle outer diameter size was chosen to be about 7.1, which makes finite size errors negligible. The digital resolution effect was analyzed by running the exact same geometry at sizes of 100^3, 200^3, and 300^3. Figure 3 shows four non-consecutive parallel slices of the 300^3 system. A full size range was only run for $E_2 = 0.1$ and 10.0, which were the limits of the shell stiffness. Other moduli were the same numerically as in 2-D. It was found that, at $E_2 = 0.1$, the resolution error was essentially zero, as all three systems gave almost exactly the same answer, within less than 0.1%. However, at $E_2 = 10.0$, there was a 3.7% drop in bulk modulus and 5.6% drop in shear modulus between the 100^3 and the 200^3 systems. There was only a 0.5% further drop in bulk modulus and 0.8% in shear modulus when going to the 300^3 system, so it was decided that the 200^3 system would give adequate accuracy for all the shell moduli. For this size system, the outer particle diameter was 28 voxel widths, while the inner diameter was 16 voxel widths.

The second 3-D system was 200^3 in size, and had two size spheres, with outer and inner particle diameters of $28 - 16$ and $14 - 8$. Judging from the data obtained on the single-sphere results, this choice should also give adequate accuracy, though it was not as carefully checked as were all the other systems. The detailed parameters used for both 3-D systems are presented in Tables 2 and 3. Figure 4 shows four parallel non-consecutive slices of the 200^3 system used.

4 D-EMT Results

The D-EMT equations were solved for the four (two 2-D, two 3-D) different microstructures for which finite element results were obtained. By varying both the microstructure and the shell stiffness, a range of data was obtained to provide a rigorous test of the D-EMT results.

Figures 5 and 6 show the comparison between the accurate finite element results for the 2-D microstructures (symbols) and the D-EMT results (lines). Both graphs show excellent agreement, with the best agreement being at the higher matrix area fraction (Fig. 6). This is not surprising, as the highest matrix area fraction has the fewest inclusions, and so is closer to the dilute limit, where the D-EMT is virtually exact. However, even for the 0.3 matrix area fraction system, Fig. 5, the agreement is still very good. Tables 4 and 5 show the actual numbers in the graphs, for closer comparison and future reference. Also note that as the matrix area fraction decreases, the moduli curves also become steeper. This is because the shell area fraction (c_2) is becoming larger, and so increasing its moduli has a greater effect on the overall moduli.

Figure 7 shows the comparision between D-EMT and finite element results for the 3-D system with one size of inclusions. The agreement is excellent, as can also be seen in Table 6. Figure 8 shows the same kind of comparison but for the two-size sphere 3-D system. The agreement in this case between D-EMT and finite element data is almost as good as in Fig. 7. The data for this case is in Table 7. It should be recalled here that the finite element results for the two-size sphere 3-D system were not checked as thoroughly as were the other systems, so there could be a larger degree of error in these results. It was found in the one-size sphere 3-D system that increasing the system size for the larger values of E_2 tended to decrease the overall moduli by a few percent. If the numerical results in Fig. 8 were to drop by only a few percent, the already good agreement would be substantially improved.

5 Discussion and Summary

One limitation of the D-EMT equations is in representing microstructure of composites. In concrete, for example, several modeling and experimental studies have shown that in a typical concrete, the shell regions are themselves percolating [36, 39, 40]. The form of D-EMT considered in this paper will not reflect this fact. The model microstructures used to test the D-EMT were carefully constructed to have non-overlapping and therefore non-percolating shell regions. However, whether or not percolation of a phase matters to the overall properties depends on the contrast of its properties with those of the surrounding phases [4, 41]. In concrete, the shell moduli probably do not differ at most from the matrix by a factor of $2-5$, which is not enough contrast for percolation to be important [4]. So this deficiency in D-EMT should not significantly affect the accuracy of D-EMT for the concrete problem. However, if a different problem were to be considered, for example fluid permeability [4], where the contrast between shell permeability and matrix permeability is on the order of 100 or more, then most likely D-EMT would fail, as the percolation of the shell regions would then be crucial. In that case, any approach not taking the thin shell layer percolation into account is unlikely to be accurate.

Since EMT is an uncertain approximation, the results of this paper are especially important in carefully showing the expected accuracy of the D-EMT equations. This paper showed that the new form of D-EMT worked very well for the class of problems considered. Using the D-EMT for a material like concrete, where the particle size distribution of the inclusions is quite a bit larger (about two orders of magnitude) than that studied here has not been tested. The main difficulty comes in finding a numerical representation of the structure using a digital image. The actual shell in concrete is also much thinner than has been considered. It is conceivable that the errors incurred using the D-EMT for a material like concrete may be significantly larger. But the excellent agreement with the numerical data found here strongly suggests that successful extensions to concrete are possible.

Tables 4–7 in this paper should be useful for other workers who wish to test various forms of EMT or other approximate formulas, by listing accurate data for the linear elastic properties of non-trivial random systems. Using the information contained in Tables 1, 2, and 3, the microstructures can be recreated easily, in case new numerical methods need to be tested. Modern computers and computer methods can now be used for the quantitative testing of approximate micromechanics theories on non-trivial, non-analytic microstructures.

This will allow a better sorting of various equations into areas of greatest usefulness, and should inspire the creation of better, more accurate choices among the various possible theories available.

Acknowledgments

We thank the Partnership for High Performance Concrete Technology of the Building and Fire Research Laboratory for partial support of the work of EJG, and the National Science Foundation Science and Technology Center for Advanced Cement-Based Materials for supporting an annual computer modeling workshop (see http://ciks.cbt.nist.gov/garboczi/) at which the authors first began to formulate their new differential effective medium theory ideas. The work of JGB was performed under the auspices of the U. S. Department of Energy by the Lawrence Livermore National Laboratory under contract No. W-7405-ENG-48 and supported specifically by the Geosciences Research Program of the DOE Office of Energy Research within the Office of Basic Energy Sciences, Division of Engineering and Geosciences.

References

[1] D. P. Bentz, E. J. Garboczi, and P.A. Stutzman, Computer modelling of the interfacial transition zone in concrete, in *Interfaces in Cementitious Composites*, edited by J.C. Maso, (E. and F.N. Spon, London, 1993), pp. 259–268. Also found at http://ciks.cbt.nist.gov/garboczi/, Chapter 6, Section 3.

[2] K. L. Scrivener, The Microstructure of Concrete, in *Materials Science of Concrete Vol. I*, edited by J. Skalny (American Ceramic Society, Westerville, OH, 1989), pp. 127–162.

[3] E. J. Garboczi and D. P. Bentz, Digital simulation of the aggregate-cement paste interfacial zone in concrete, J. Mater. Res. 6, 196–201 (1991).

[4] J. D. Shane, T. O. Mason, H. M. Jennings, E. J. Garboczi, and D. P. Bentz, Effect of the interfacial transition zone on the conductivity of portland cement mortars, J. Amer. Ceram. Soc., in press (1999).

[5] D. P. Bentz, P. A. Stutzman, and E. J. Garboczi, Experimental and simulation studies of the interfacial zone in concrete, Cem. Conc. Res. **22**, 891–902 (1992).

[6] E. J. Garboczi and D. P. Bentz, Analytical formulas for interfacial transition zone properties, Advanced Cement-Based Materials **6**, 99–108 (1997).

[7] E. Herve and A. Zaoui, n-Layered inclusion-based micromechanical modelling, Int. J. Eng. Sci. **31**, 1–10 (1993).

[8] P. L. Iske, N. K. J. Sterk, J. Oortwijn, Effective elastic properties of suspensions of radially symmetric particles, Physica A **209**, 96–128 (1994).

[9] M. P. Lutz and P. J. M. Monteiro, Effect of the transition zone on the bulk modulus of concrete, in *Microstructure of Cement-Based Systems/Bonding and Interfaces in Cementitious Materials Vol. 370*, edited by S. Diamond, S. Mindess, F.P. Glasser, L.W. Roberts, J.P. Skalny, and L.D. Wakeley (Materials Research Society, Pittsburgh, 1995), pp. 413–418.

[10] E.J. Garboczi and D.P. Bentz, Multi-scale analytical/numerical theory of the diffusivity of concrete, Advanced Cement-Based Materials **8**, 77–88 (1998).

[11] D.P. Bentz, E.J. Garboczi, and E.S. Lagergren, Multi-scale microstructural modelling of concrete diffusivity: Identification of significant variables, Cement, Concrete, and Aggregates **20**, 129–139 (1998).

[12] M. P. Cleary, I. W. Chen, and S. M. Lee, Self-consistent techniques for heterogeneous media, J. Engineering Mech. Div. — ASCE **106**, 861–887 (1980).

[13] P. Sheng and A. J. Callegari, Differential effective medium theory of sedimentary rocks, Appl. Phys. Lett. **44**, 738–740 (1984).

[14] A. N. Norris, A differential scheme for the effective moduli of composites, Mech. Materials **4**, 1–16 (1985).

[15] P. Sheng, Effective medium theory of sedimentary rocks, Phys. Rev. B **41**, 4507–4512 (1990).

[16] P. Sheng, Consistent modeling of the electrical and elastic properties of sedimentary rocks, Geophysics **56**, 1236–1243 (1991).

[17] J. Dvorkin, J. Berryman, and A. Nur, Elastic moduli of cemented sphere packs, Mech. Materials **31**, 461–469 (1999).

[18] L. M. Schwartz, E. J. Garboczi, and D. P. Bentz, Interfacial transport in porous media: Application to D.C. electrical conductivity of mortars, Journal of Applied Physics **78**, 5898–5908 (1995). Note misprint in eq. 3.1. The corrected form is given here as eq. (8).

[19] E. J. Garboczi and J. G. Berryman, New effective medium theory for the diffusivity or conductivity of a multi-scale concrete microstructure model, submitted to Conc. Sci. and Engin., (2000).

[20] R. M. Christensen and K. H. Lo, Solutions for effective shear properties in three phase sphere and cylinder models, J. Mech. Phys. Solids **27**, 315–330 (1979).

[21] R. M. Christensen, *Mechanics of Composite Materials*, Wiley, New York, 1979, pp. 47–58.

[22] G. W. Milton, The coherent potential approximation is a realizable effective medium scheme, Commun. Math. Phys. **99**, 463–500 (1985).

[23] R. Hill, Elastic properties of reinforced solids: Some theoretical principles, J. Mech. Phys. Solids **11**, 357–372 (1963).

[24] E. J. Garboczi, Finite element and finite difference programs for computing the linear electric and elastic properties of digital images of random materials, NIST Internal Report 6269 (1998). Also available at http://ciks.cbt.nist.gov/garboczi/, Chapter 2.

[25] E. J. Garboczi and A. R. Day, An algorithm for computing the effective linear elastic properties of heterogeneous materials: 3-D results for composites with equal phase Poisson ratios, J. Mech. Phys. Solids **43**, 1349–1362 (1995).

[26] J. G. Berryman, Mixture Theories for Rock Properties, in *Rock Physics and Phase Relations-A Handbook of Physical Constants*, edited by T.J. Ahrens (American Geophysical Union, Washington DC, 1995), pp. 205–228.

[27] R. McLaughlin, A study of the differential scheme for composite materials, Int. J. Eng. Sci. **15**, 237–244 (1977).

[28] P. A. Berge, J. G. Berryman, and B. P. Bonner, Influence of microstructure on rock elastic properties, Geophys. Res. Lett. **20**, 2619–2622 (1993).

[29] W. Xia and M. F. Thorpe, Percolation properties of random ellipses, Phys. Rev. A **38**, 2650 (1988).

[30] S. Torquato, Random heterogeneous media: Microstructure and improved bounds on effective properties, Appl. Mech. Rev. **44**, 37–76 (1991).

[31] J. F. Douglas and E. J. Garboczi, Intrinsic viscosity and polarizability of particles having a wide range of shapes, Adv. Chem. Phys. 91, 85–153 (1995).

[32] Z. Hashin, The elastic moduli of heterogeneous materials, J. Appl. Mech. **29**, 143–150 (1962).

[33] R. M. Christensen, A critical evaluation for a class of micromechanics models, J. Mech. Phys. Solids **38**, 379–404 (1990).

[34] F. B. Hildebrand, *Introduction to Numerical Analysis*, Dover, New York, 1956, pp. 285–292.

[35] W. H. Press, B. P. Flannery, S. A. Teukolsky, and W. T. Vetterling, *Numerical Recipes in C*, Cambridge University Press, Cambridge, 1988, pp. 566–573.

[36] D. N. Winslow, M. D. Cohen, D. P. Bentz, K. A. Snyder, and E. J. Garboczi, Percolation and porosity in mortars and concretes, Cem. Conc. Res. **24**, 25–37 (1994).

[37] http://ciks.cbt.nist.gov/garboczi/, Chapter 7, Section 4b.

[38] A. P. Roberts and E. J. Garboczi, Elastic properties of model porous ceramics, submitted to J. Amer. Ceram. Soc. (1999).

[39] D.P. Bentz, E.J. Garboczi, and K.A. Snyder, A hard-core soft shell microstructural model for studying percolation and transport in three-dimensional composite media, NIST Internal Report 6265 (1999). Also available at http://ciks.cbt.nist.gov/garboczi/, Chapter 6, Section 8.

[40] K. L. Scrivener and K. M. Nemati, The percolation of pore space in the cement paste/aggregate interfacial zone of concrete, Cem. Conc. Res. **26**, 35–40 (1996).

[41] E. J. Garboczi, K. A. Snyder, J. F. Douglas, and M.F. Thorpe, Geometrical percolation threshold of overlapping ellipsoids, Phys. Rev. E **52**, 819–828 (1995).

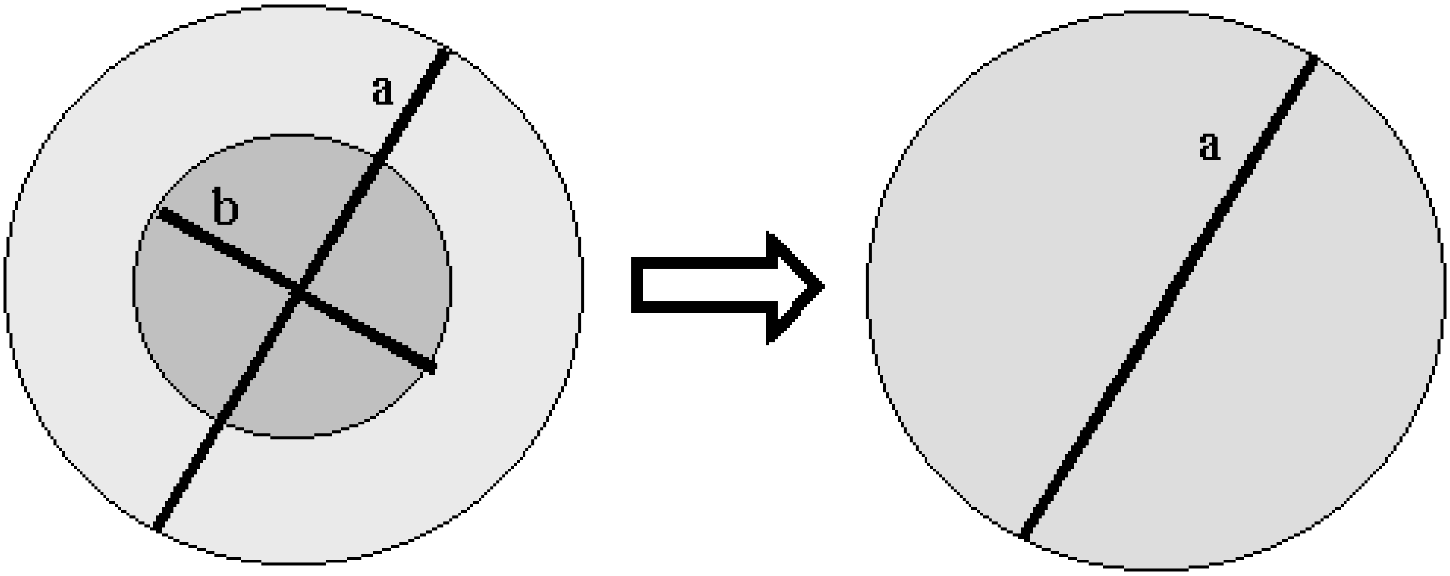

Figure 1: The mapping of a composite inclusion particle into an effective particle whose diameter is the diameter of the outer shell. The figure shows a cross-section of a sphere (or a circle) taken through the center.

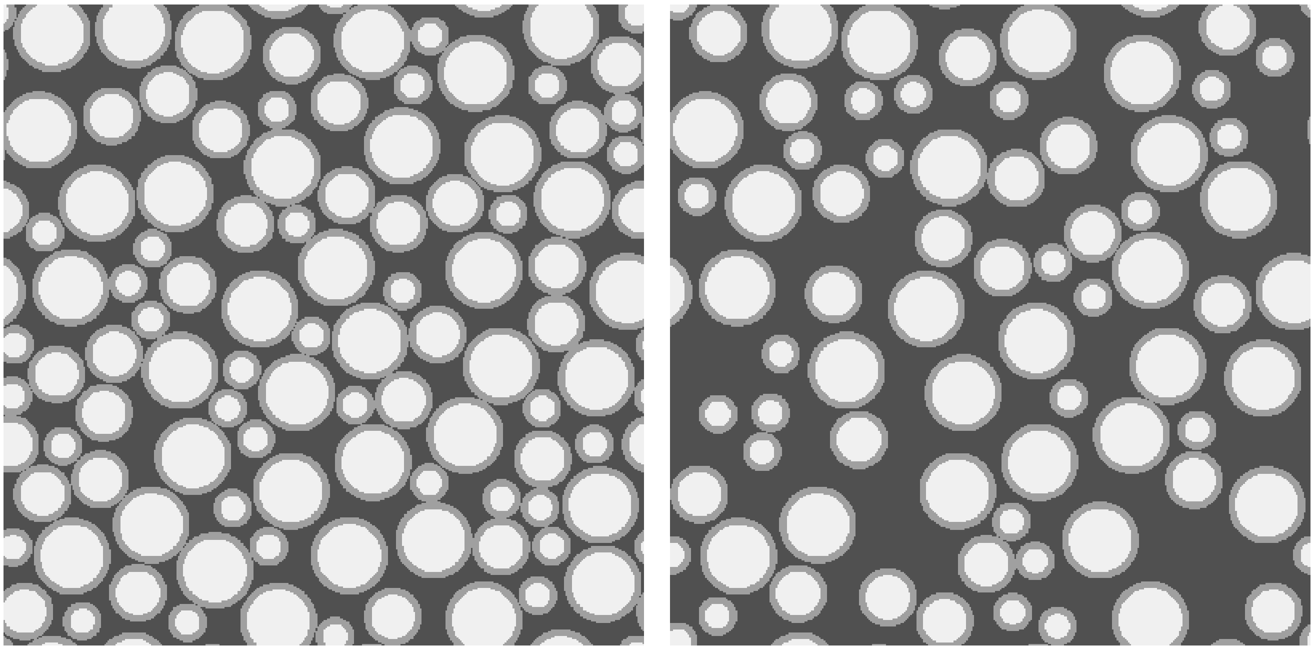

Figure 2: Gray-scale pictures of the 2-D models used to test the D-EMT predictions. Using concrete language, the dark gray is the matrix, the middle gray is ITZ, and the lightest gray phase is the bulk matrix phase. There are three sizes of aggregates in this picture, and the matrix area fraction is 0.3 (left) and 0.5 (right).

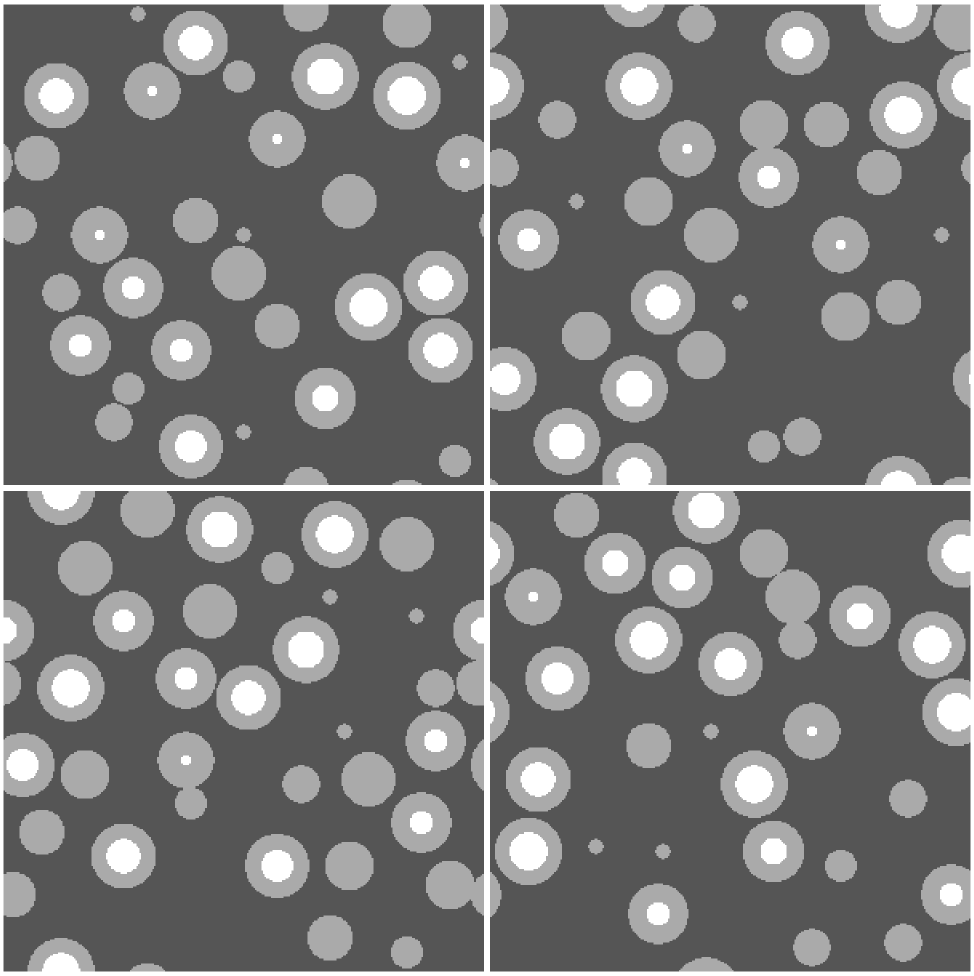

Figure 3: Four 300^3 slices from the 3-D monosize sphere model used to test the D-EMT predictions. Using concrete language, the dark gray is the matrix, the middle gray is ITZ, and the lightest gray phase is the bulk matrix phase. The matrix volume fraction is 0.668.

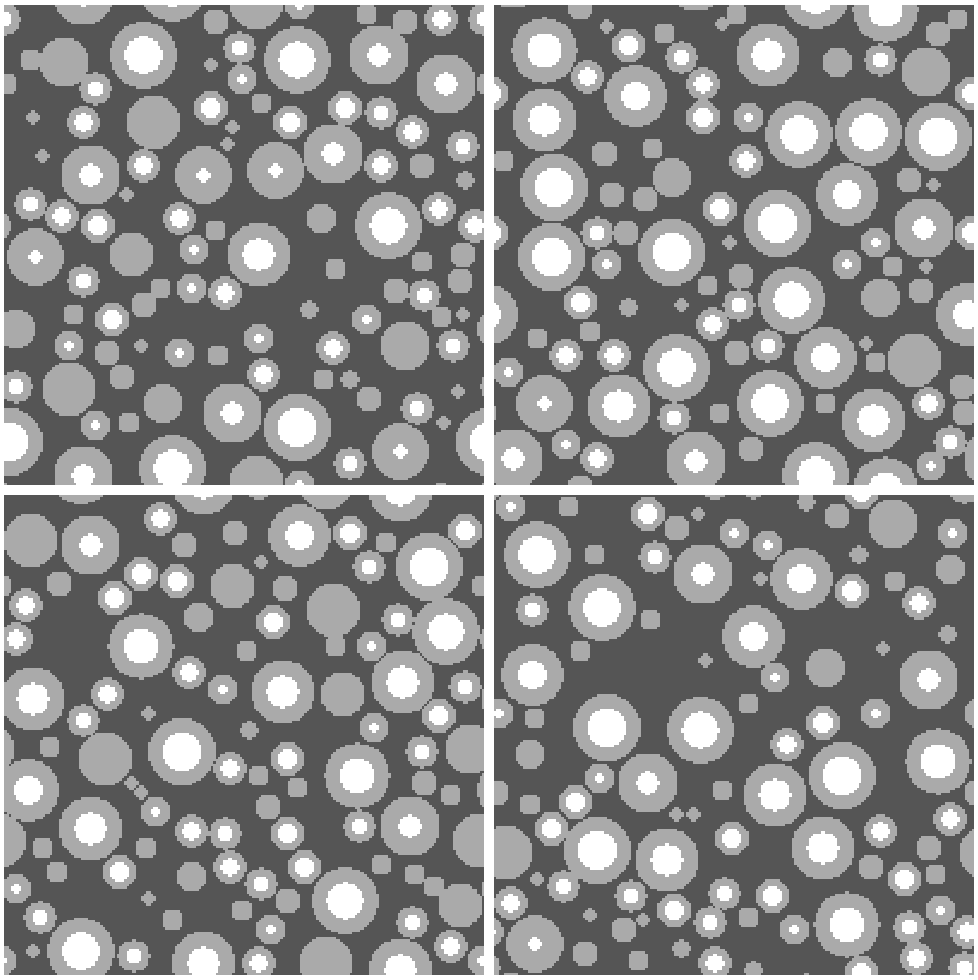

Figure 4: Four 200^3 slices from the 3-D two size sphere model used to test the D-EMT predictions. Using concrete language, the dark gray is the matrix, the middle gray is ITZ, and the lightest gray phase is the bulk matrix phase. The matrix volume fraction is 0.517.

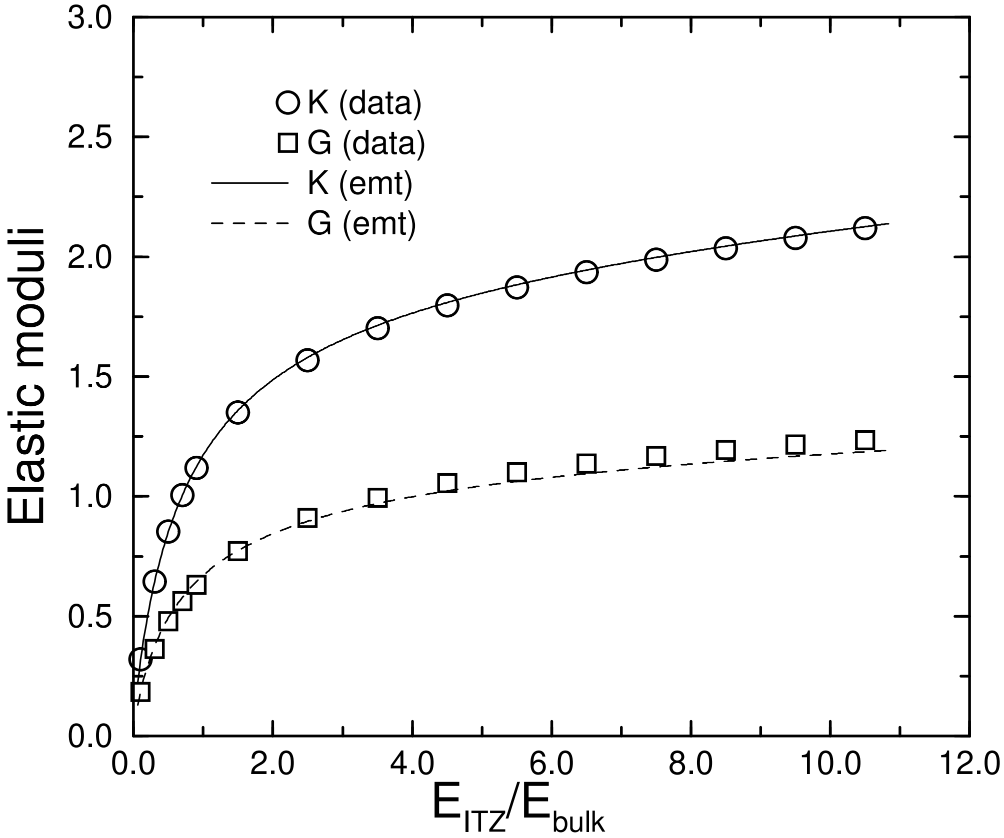

Figure 5: Showing the D-EMT results for K and G compared to the numerical results for the 2-D 0.3 matrix area fraction model. The abscissa is E_2/E_1.

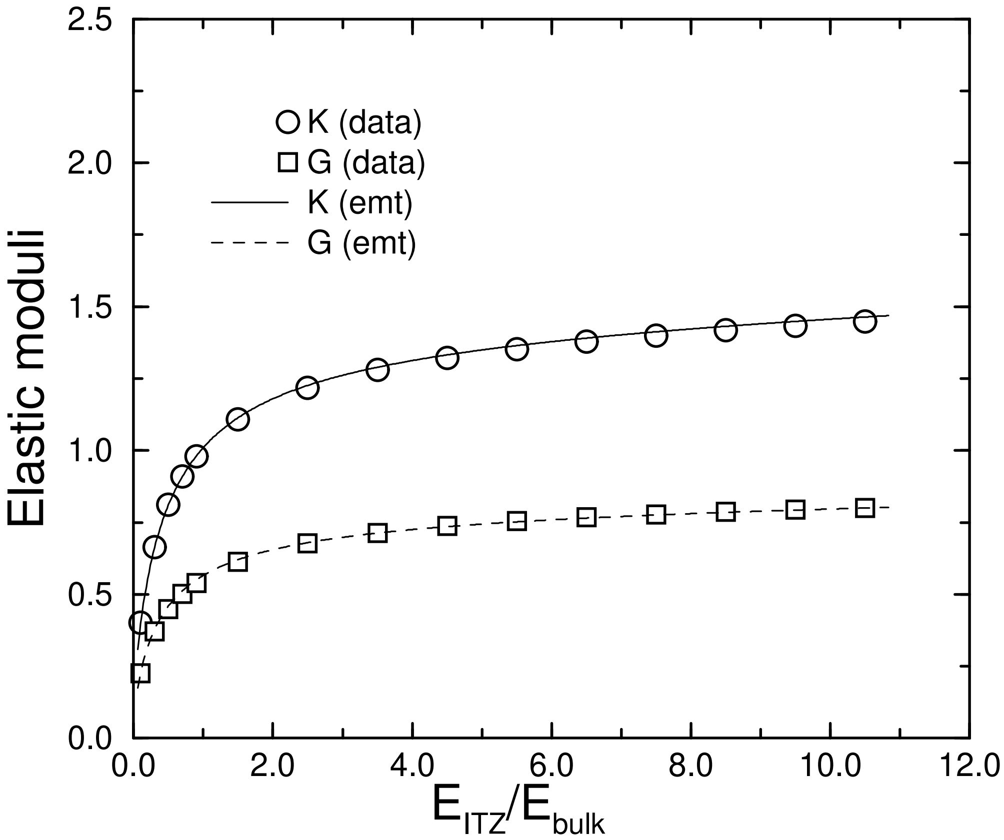

Figure 6: Showing the D-EMT results for K and G compared to the numerical results for the 2-D 0.5 matrix area fraction model. The abscissa is E_2/E_1.

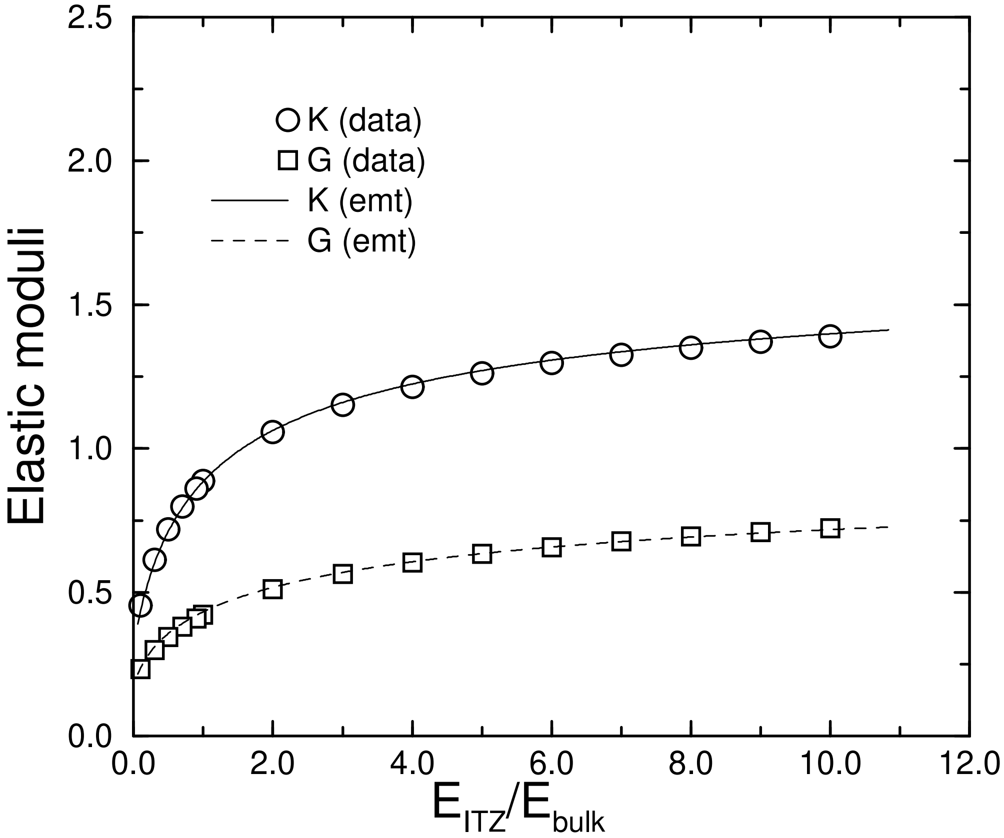

Figure 7: Showing the D-EMT results for K and G compared to the numerical results for the monosize sphere 3-D model. The matrix volume fraction was 0.668. The abscissa is E_2/E_1.

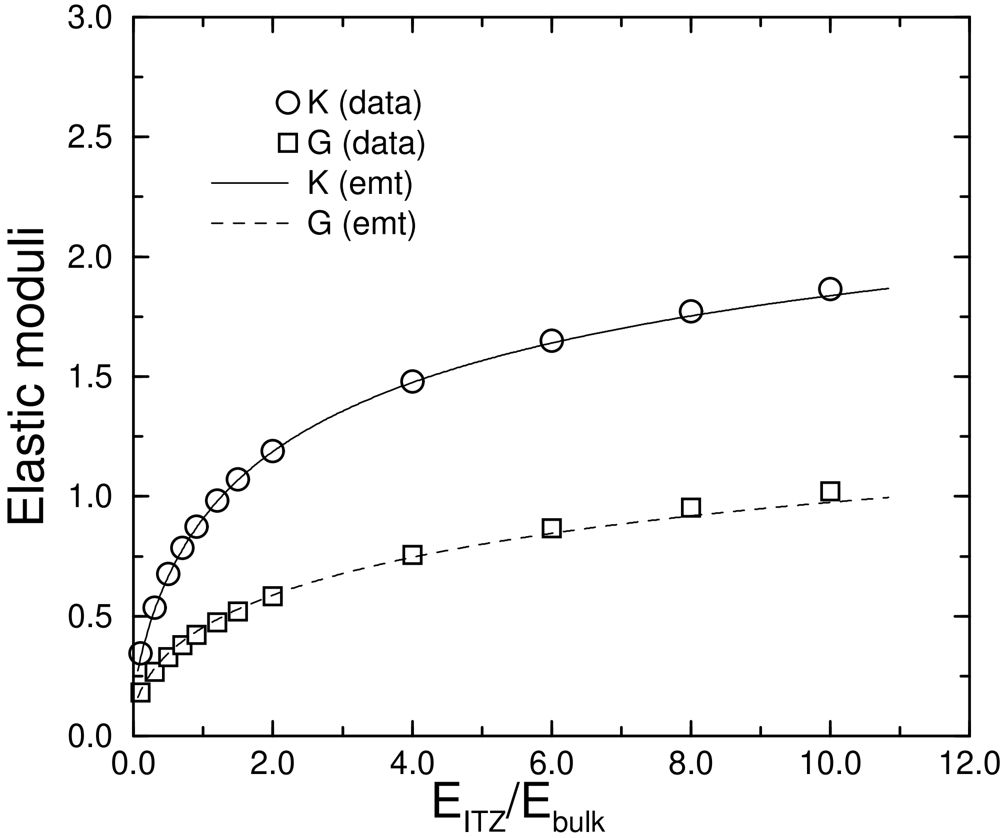

Figure 8: Showing the D-EMT results for K and G compared to the numerical results for the two size sphere 3-D model. The matrix volume fraction was 0.517.The abscissa is E_2/E_1.

Table 1: Parameters defining the 2-D microstructures. N = number, L = large circles, M = medium circles, S = small circles, and c is area fraction. Phase 1 is the inner circle, phase 3 is the matrix, and phase 2 is the shell material.

N_L	N_M	N_S	c_1	c_2	c_3
36	28	35	0.303	0.275	0.422
26	20	25	0.499	0.198	0.303

Table 2: Parameters defining the 3-D microstructures, which had either one or two sizes of spheres. The numbers are all for 200^3 systems. N = number, L = large spheres, S = small spheres, and c is volume fraction. Phase 1 is the inner sphere, phase 3 is the matrix, and phase 2 is the shell material.

N_L	N_S	c_1	c_2	c_3
230		0.668	0.269	0.063
220	900	0.517	0.392	0.091

Table 3: Areas of circles and volumes of spheres used in pixels and voxels.

Circle diameter	Sphere diameter	Area ($pixel\,\#$)	Volume ($voxel\,\#$)
121		11476	
99		7668	
91		6488	
69		3720	
61		2912	
39		1184	
	28		11536
	16		2176
	14		1472
	8		280

Table 4: A list of numerical data and D-EMT results for the 2-D, 0.3 matrix area fraction system.

E_2/E_1	K(data)	K(D-EMT)	G(data)	G(D-EMT)
0.1	0.320	0.319	0.186	0.187
0.3	0.645	0.643	0.364	0.378
0.5	0.855	0.854	0.479	0.495
0.7	1.005	1.006	0.564	0.580
0.9	1.120	1.123	0.631	0.644
1.5	1.351	1.360	0.772	0.775
2.5	1.568	1.580	0.910	0.897
3.5	1.702	1.714	0.995	0.971
4.5	1.797	1.809	1.055	1.023
5.5	1.872	1.883	1.101	1.063
6.5	1.935	1.944	1.138	1.096
7.5	1.988	1.997	1.168	1.123
8.5	2.036	2.044	1.194	1.147
9.5	2.079	2.086	1.216	1.168
10.5	2.119	2.125	1.236	1.186

Table 5: A list of numerical data and D-EMT results for the 2-D, 0.5 matrix area fraction system.

E_2/E_1	K(data)	K(D-EMT)	G(data)	G(D-EMT)
0.1	0.401	0.397	0.226	0.227
0.3	0.665	0.663	0.370	0.378
0.5	0.812	0.811	0.449	0.460
0.7	0.910	0.910	0.502	0.513
0.9	0.979	0.981	0.540	0.551
1.5	1.109	1.114	0.614	0.621
2.5	1.218	1.226	0.677	0.680
3.5	1.280	1.289	0.713	0.713
4.5	1.321	1.332	0.737	0.735
5.5	1.353	1.365	0.755	0.752
6.5	1.378	1.391	0.768	0.765
7.5	1.399	1.413	0.778	0.776
8.5	1.418	1.432	0.787	0.785
9.5	1.434	1.449	0.795	0.793
10.5	1.449	1.464	0.801	0.800

Table 6: A list of numerical data and D-EMT results for the 3-D, 0.668 matrix volume fraction, one sphere system (Fig. 7).

E_2/E_1	K(data)	K(D-EMT)	G(data)	G(D-EMT)
0.1	0.455	0.436	0.233	0.238
0.3	0.613	0.602	0.300	0.311
0.5	0.720	0.713	0.346	0.357
0.7	0.799	0.795	0.381	0.392
0.9	0.861	0.858	0.410	0.420
1.0	0.887	0.886	0.422	0.432
2.0	1.058	1.063	0.510	0.517
3.0	1.157	1.160	0.565	0.569
4.0	1.214	1.224	0.603	0.606
5.0	1.260	1.271	0.633	0.635
6.0	1.296	1.307	0.657	0.657
7.0	1.326	1.336	0.678	0.676
8.0	1.350	1.360	0.695	0.692
9.0	1.371	1.381	0.710	0.706
10.0	1.390	1.399	0.723	0.718

Table 7: A list of numerical data and D-EMT results for the 3-D, 0.517 matrix volume fraction, two sphere system (Fig. 8).

E_2/E_1	K(data)	K(D-EMT)	G(data)	G(D-EMT)
0.1	0.346	0.327	0.183	0.189
0.3	0.537	0.526	0.269	0.283
0.5	0.676	0.668	0.331	0.346
0.7	0.785	0.779	0.381	0.396
0.9	0.874	0.869	0.423	0.437
1.2	0.983	0.980	0.476	0.487
1.5	1.071	1.075	0.521	0.533
2.0	1.189	1.187	0.584	0.589
4.0	1.479	1.475	0.755	0.746
6.0	1.650	1.639	0.868	0.846
8.0	1.772	1.753	0.953	0.919
10.0	1.866	1.837	1.022	0.975